Dynamics of Colombo's Top: Tidal Dissipation and Resonance Capture

Yubo Su,[1]* Dong Lai[1,2]

[1] *Cornell Center for Astrophysics and Planetary Science, Department of Astronomy, Cornell University, Ithaca, NY 14853, USA*
[2] *Tsung-Dao Lee Institute & School of Physics and Astronomy, Shanghai Jiao Tong University, 200240 Shanghai, China*

ABSTRACT
Abstract here

Key words: planet-star interactions

1 INTRODUCTION

• Studying planetary obliquities (define) is important. Cassini States are key. More introduction.

• Resonance capture via separatrix crossing was first considered by (Henrard 1982) for non-dissipative perturbations (e.g. Su & Lai 2020). However, tidal friction is dissipative, so this formalism does not apply. We generalize this calculation and show that it reproduces results.

In Section XXX. . .

2 SPIN EVOLUTION EQUATIONS AND CASSINI STATES: REVIEW

In this section, we first briefly lay out the spin dynamics of the planet, introducing the Cassini State spin-orbit resonance (for more details, see Su & Lai 2020). We then introduce the weak friction theory of equilibrium tides used in this work (Lai 2012). While many different tidal effects may dominate in different planetary systems, our qualitative conclusions do not depend on the specific form of the tidal dissipation, so we use the classic weak friction theory for simplicity.

2.1 Spin Dynamics in the Absence of Tides

2.1.1 Equations of Motion

We consider a star of mass $M_\star$ hosting an inner oblate planet of mass m and radius R on a circular orbit with semi-major axis a and an outer perturber of mass m_p on a circular orbit with semi-major axis a_p. We assume that the two orbits are mildly misaligned with mutual inclination I. Denote $\mathbf{S}$ the spin angular momentum and $\mathbf{L}$ the orbital angular momentum of the planet, and $\mathbf{L}_p$ the angular momentum of the perturber. The corresponding unit vectors are $\hat{\mathbf{s}} \equiv \mathbf{S}/S$, $\hat{\mathbf{l}} \equiv \mathbf{L}/L$, and $\hat{\mathbf{l}}_p \equiv \mathbf{L}_p/L_p$. The spin axis $\hat{\mathbf{s}}$ of the planet tends to precess around its orbital (angular momentum) axis $\hat{\mathbf{l}}$, driven by the gravitational torque from the host star acting on the planet's rotational bulge. On the other hand, $\hat{\mathbf{l}}$ and the disk axis $\hat{\mathbf{l}}_p$ precess around each other due to gravitational interactions. We assume $S \ll L \ll L_p$, so $\hat{\mathbf{l}}_p$ and $\hat{\mathbf{l}}$

* E-mail: yubosu@astro.cornell.edu

are nearly constant. The equations of motion for $\hat{\mathbf{s}}$ and $\hat{\mathbf{l}}$ in this limit are (Anderson & Lai 2018; Su & Lai 2020)

$$\frac{d\hat{\mathbf{s}}}{dt} = \omega_{sl} \left(\hat{\mathbf{s}} \cdot \hat{\mathbf{l}}\right) \left(\hat{\mathbf{s}} \times \hat{\mathbf{l}}\right) \equiv \alpha \left(\hat{\mathbf{s}} \cdot \hat{\mathbf{l}}\right) \left(\hat{\mathbf{s}} \times \hat{\mathbf{l}}\right), \tag{1}$$

$$\frac{d\hat{\mathbf{l}}}{dt} = \omega_{lp} \left(\hat{\mathbf{l}} \cdot \hat{\mathbf{l}}_p\right) \left(\hat{\mathbf{l}} \times \hat{\mathbf{l}}_p\right) \equiv -g \left(\hat{\mathbf{l}} \times \hat{\mathbf{l}}_p\right), \tag{2}$$

where

$$\omega_{sl} \equiv \frac{3 G J_2 m R^2 M_\star}{2 a^3 I \Omega_s} = \frac{3 k_q}{2 k} \frac{M_\star}{m} \left(\frac{R}{a}\right)^3 \Omega_s, \tag{3}$$

$$\omega_{lp} = \frac{3 m_p}{4 M_\star} \left(\frac{a}{a_p}\right)^3 n. \tag{4}$$

In Eq. (3), Ω_s is the spin frequency of the inner planet, $I = k m R^2$ (with k a constant) is its moment of inertia and $J_2 = k_q \Omega_s^2 (R^3/Gm)$ (with k_q a constant) is its rotation-induced (dimensionless) quadrupole moment [for a body with uniform density, $k = 0.4$, $k_q = 0.5$; for rocky planets, $k \simeq 0.2$ and $k_q \simeq 0.17$ (e.g. Lainey 2016) ? not sure]. In other studies, $3k_q/2k$ is often notated as $k_2/2C$ (e.g. Millholland & Batygin 2019). In Eq. (4), $n \equiv \sqrt{GM_\star/a^3}$ is the inner planet's orbital mean motion, and we have assumed $a_p \gg a$ and included only the leading-order (quadrupole) interaction between the inner planet and perturber. Following standard notation, we define $\alpha = \omega_{sl}$ and $g \equiv -\omega_{lp} \cos I$ (e.g. Colombo 1966).

As in Su & Lai (2020), we combine Eqs. (1–2) into a single equation by transforming into a frame rotating about $\hat{\mathbf{l}}_p$ with frequency g. In this frame, $\hat{\mathbf{l}}_p$ and $\hat{\mathbf{l}}$ are both fixed, and $\hat{\mathbf{s}}$ evolves as:

$$\left(\frac{d\hat{\mathbf{s}}}{dt}\right)_{rot} = \alpha \left(\hat{\mathbf{s}} \cdot \hat{\mathbf{l}}\right) \left(\hat{\mathbf{s}} \times \hat{\mathbf{l}}\right) + g \left(\hat{\mathbf{s}} \times \hat{\mathbf{l}}_p\right). \tag{5}$$
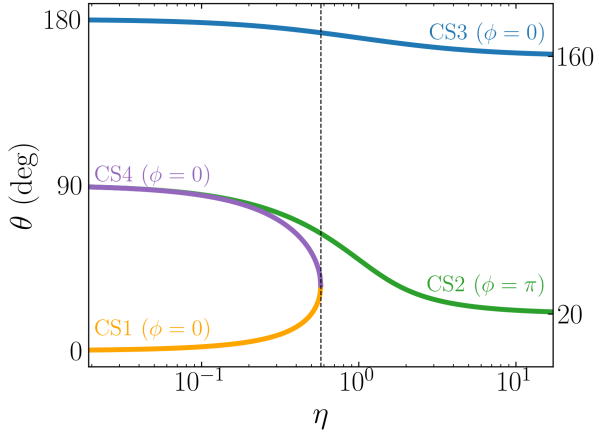
In this reference frame, we choose the coordinate system such that $\hat{\mathbf{z}} = \hat{\mathbf{l}}$ and $\hat{\mathbf{l}}_p$ lies in the $\hat{\mathbf{x}}$-$\hat{\mathbf{z}}$ plane. We describe $\hat{\mathbf{s}}$ in spherical coordinates using the polar angle θ, the planet's obliquity, and ϕ, the precessional phase of $\hat{\mathbf{s}}$ about $\hat{\mathbf{l}}$.

The equilibria of Eq. (5) are referred to as *Cassini States* (CSs; Colombo 1966; Peale 1969). We follow the notation of Su & Lai (2020), where the parameter

$$\eta \equiv -\frac{g}{\alpha}, \tag{6}$$

is used. For a given value of η, there can be either two or four CSs, all of which require $\hat{\mathbf{s}}$ lie in the plane of $\hat{\mathbf{l}}$ and $\hat{\mathbf{l}}_p$. Following the standard

Figure 1. Cassini State obliquities θ as a function of $\eta \equiv -g/\alpha$ (Eq. 6) for $I = 20°$. The vertical dashed line denotes η_c, where the number of Cassini States changes from four to just two (Eq. 7). The y-axis labels on the right of the plot show the asymptotic obliquities for CS2 and CS3, I and $180° - I$ respectively. Note that θ does not follow the standard convention (e.g. Colombo 1966) and is simply the angle between $\hat{\mathbf{s}}$ and $\hat{\mathbf{I}}$.

nomenclature, $\hat{\mathbf{s}}$ and $\hat{\mathbf{I}}_p$ are on opposite sides of $\hat{\mathbf{I}}$ for CSs 1, 3, and 4, and are on the same side for CS2. We depart from the standard convention and simply label the CSs in spherical coordinates: figure 1 shows the CS obliquities as a function of η. CS1 and CS4 do not exist when $\eta > \eta_c$, where

$$\eta_c \equiv \left(\sin^{2/3} I + \cos^{2/3} I \right)^{-3/2} . \tag{7}$$

The Hamiltonian corresponding to Eq. (5) is

$$
\begin{aligned}
H &= -\frac{\alpha}{2} \left(\hat{\mathbf{s}} \cdot \hat{\mathbf{I}} \right)^2 - g \left(\hat{\mathbf{s}} \cdot \hat{\mathbf{I}}_d \right) \\
&= -\frac{\alpha}{2} \cos^2 \theta - g \left(\cos \theta \cos I - \sin I \sin \theta \cos \phi \right) .
\end{aligned}
\tag{8}
$$

Here, $\cos \theta$ and ϕ form a canonically conjugate pair of variables. Figure 2 shows the level curves of this Hamiltonian for $I = 20°$, for which $\eta_c \approx 0.574$ (Eq. 7). When $\eta < \eta_c$, CS4 exists and is a saddle point. The two trajectories originating and ending at CS4 are the only two infinite-period orbits in the phase space. Together, these two critical trajectories are referred to as the *separatrix* and divide phase space into three zones. Trajectories in zone II librate about CS2 while those in zones I and III circulate. On the other hand, when $\eta > \eta_c$, all trajectories circulate. When the separatrix exists, we divide it into two curves: C_+, the boundary between zones I and II, and C_-, the boundary between zones II and III.

3 SPIN EVOLUTION WITH ALIGNMENT TORQUE

In this section, we consider a simplified model of equilibrium tides that isolates the important new phenomenon presented in this paper. We assume that the spin magnitude of the planet is constant, so α and g are both fixed, while the spin orientation $\hat{\mathbf{s}}$ experiences an alignment torque towards $\hat{\mathbf{I}}$ on the alignment timescale t_s:

$$\left(\frac{d\hat{\mathbf{s}}}{dt} \right)_{\text{tide}} = \frac{1}{t_s} \hat{\mathbf{s}} \times \left(\hat{\mathbf{I}} \times \hat{\mathbf{s}} \right) . \tag{9}$$
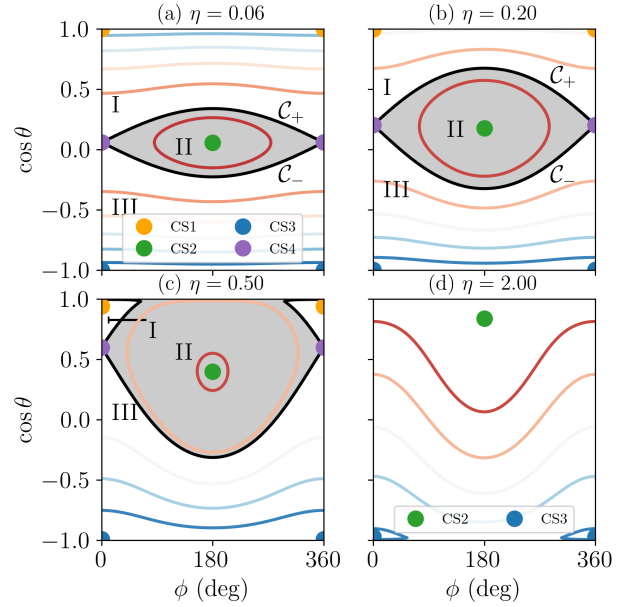
Figure 2. Level curves of the Cassini State Hamiltonian (Eq. 8) for $I = 20°$, for which $\eta_c \approx 0.57$ (Eq. 7). For $\eta < \eta_c$, there are four Cassini States (labeled), while for $\eta > \eta_c$ there are only two. In the former case, the existence of a *separatrix* (solid black lines) separates phase space into three numbered zones (I/II/III, labeled). We denote the upper and lower legs of the separatrix by $C_\pm$ respectively, as shown in the upper two panels.

The full equations of motion for $\hat{\mathbf{s}}$ in the coordinates θ and ϕ can be written:

$$\frac{d\theta}{dt} = -g \sin I \sin \phi - \frac{1}{t_s} \sin \theta, \tag{10}$$

$$\frac{d\phi}{dt} = -\alpha \cos \theta - g \left(\cos I + \sin I \cot \theta \cos \phi \right) . \tag{11}$$

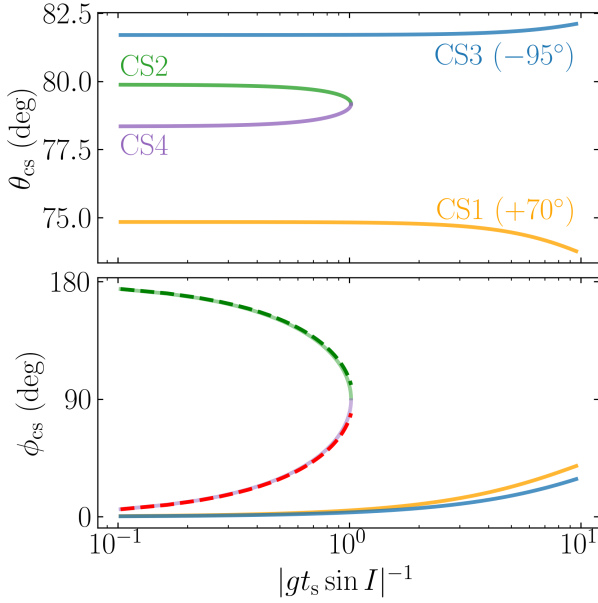### 3.1 Shifted Cassini States and Linear Stability Analysis

If the alignment torque is weak ($|gt_s| \gg 1$), then the fixed points of Eqs. (10–11) are just slightly shifted CSs. This shift can be calculated cleanly to leading order: all of the CS obliquities θ_{cs} are unchanged while the azimuthal angle ϕ_{cs} for each CS now satisfies

$$\sin \phi_{cs} = \frac{\sin \theta_{cs}}{\sin I |g| t_s} . \tag{12}$$

We can see that if $t_s > t_{s,c}$, where

$$t_{s,c} = \frac{1}{|g| \sin I}, \tag{13}$$

then Eq. (12) will always have solutions for ϕ_{cs}, and the alignment torque never changes the number of fixed points of the system. If t_s is decreased below $t_{s,c}$, CS2 and CS4 cease to be fixed points if $\eta \ll 1$ (as first noted in Fabrycky et al. 2007), as $\theta_{cs} \approx 90°$ for these (see Fig. 1), while the other CSs have small $\sin \theta_{cs}$ and are only slightly perturbed. Figure 3 shows the obliquity and azimuthal angles for each of the CSs in the $\eta \ll 1$ case, where it can be seen that CS2 and CS4 collide and annihilate. The phase shift ϕ_{cs} for CS2 and CS4 for $t_s > t_{s,c}$ can be predicted to good accuracy using Eq. (12) using $\theta_{cs} \approx \pi/2 - \eta \cos(I) \approx 79°$ (Su & Lai 2020) for both, shown as the dashed lines in the bottom panel of Fig. 3. For the remainder of this

Figure 4. λ_0^2 (Eq. 16) as a function of η for the four CSs. The solid lines give λ_0^2 for the unperturbed ϕ_{cs}, and the dashed lines give the values for ϕ_{cs} shifted by 60° ($\phi_{cs} = 120°$ for CS2 and $\phi_{cs} = 60°$ for CSs 1, 3, and 4).

3.2 Spin Obliquity Evolution Driven by Alignment Torque

With the above results, we are equipped to ask questions about the dynamics of Eqs. (10–11): what is the long term behavior for a general initial $\hat{s}$? If $\eta > \eta_c$, then the only possible final spin state is CS2, and all initial conditions will evolve asympotically towards it. As such, we consider only $\eta < \eta_c$, where an initial condition can asymptotically evolve towards either CS1 or CS2. We numerically integrate Eqs. (10–11) for many random initial conditions uniformly distributed in $(\cos\theta, \phi)$ with $|g| t_s = 10^{-3}$ and record the nearest CS for each integration after $10 t_s$. In Fig. 5, we show the results of this procedure for $\eta = 0.2$, and $I = 20°$. It is clear that initial conditions in zone I evolve into CS1, those in zone II evolve into CS2, while those in zone III have a probabilistic outcome. We aim to understand each of these in turn:

For initial conditions in zone I, the spin circulates, and $\dot{\theta}$ is negative everywhere during the cycle. Thus, for initial conditions in zone I, θ decreases until the trajectory has converged to CS1. This is intuitively reasonable, as CS1 is stable.

For initial conditions in zone II, our stability calculation in Section 3.1 shows that initial conditions sufficiently near CS2 will converge to CS2. In fact, this result can be extended to all initial conditions inside the separatrix; see Appendix A.

For initial conditions in zone III, since there are no stable CSs in zone III, the system must evolve through the separatrix to reach one of either CS1 or CS2. The outcome of the separatrix encounter is effectively probabilistic and determines the final CS. Intuitively, this can be understood as probabilistic resonance capture: since $\eta \ll \eta_c$, $\alpha \gg -g$ (the spin-orbit precession rate, Eq. 1, and the orbit precession induced by the perturber, Eq. 2, respectively), but $\alpha \cos\theta$ can become commensurate with $-g$ if $\cos\theta \sim \eta$. This is achieved as θ evolves from an initially retrograde obliquity through 90° towards 0° under the influence of the dissipative term in Eq. (10).

While similar in behavior to previous studies of probabilistic resonance capture (Henrard 1982; Su & Lai 2020), the underlying mechanism is different: in these previous studies, the phase space structure itself evolves and causes systems to transition among phase space zones, while in the present scenario, a non-Hamiltonian, dissipative

Figure 3. Modified CS obliquities (top) and azimuthal angles (bottom) for $I = 20°$ and $\eta = 0.2$, where the CS1 and CS3 obliquities have been offset (labeled in top legend) to improve clarity of the plot. In both panels, the solid lines give the result when applying a numerical root finding algorithm to the full equations of motion, Eqs. (10–11), while the dotted lines in the bottom panel give the CS2 and CS4 azimuthal angles according to Eq. (12). At $|g t_s \sin I| = 1$, CS2 and CS4 collide and annihilate (Eq. 13).

section, we will consider the case where $t_s \gg t_{s,c}$ and the CSs only differ slightly from their unperturbed locations.

We next seek to characterize the stability of small perturbations about each of the CSs in the presence of the weak tidal alignment torque. We can linearize Eqs. (10–11) about a shifted CS, yelding

$$\frac{d}{dt}\begin{bmatrix}\theta\\\phi\end{bmatrix} = \begin{bmatrix}-\dfrac{\cos\theta}{t_s} & -g\sin I\cos\phi\\ \alpha\sin\theta + g\dfrac{\sin I\cos\phi}{\sin^2\theta} & 0\end{bmatrix}_{cs}\begin{bmatrix}\Delta\theta\\\Delta\phi\end{bmatrix}, \qquad (14)$$

where the cs subscript indicates evaluating at a CS, $\Delta\theta = \theta - \theta_{cs}$, and $\Delta\phi = \phi - \phi_{cs}$. The eigenvalues λ of Eq. (14) satisfy the equation

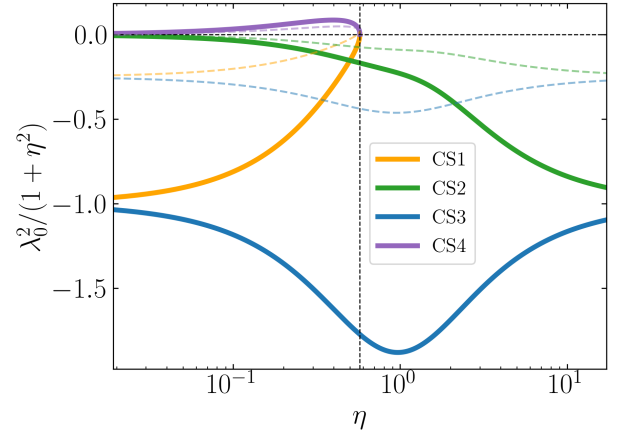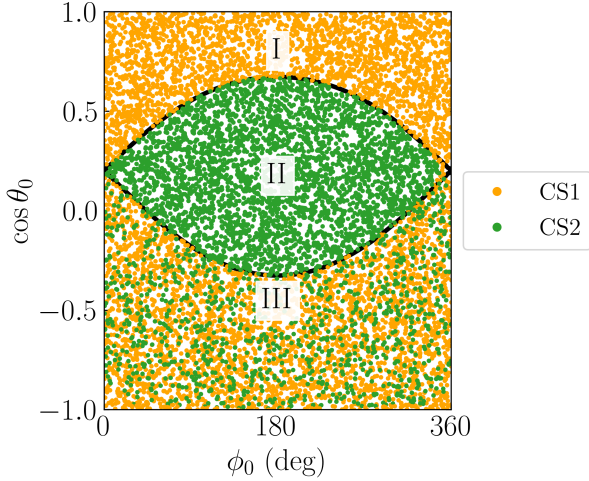$$0 = \left(\lambda + \frac{\cos\theta_{cs}}{t_s}\right)\lambda - \lambda_0^2, \qquad (15)$$

where

$$\lambda_0^2 \equiv \left(\alpha\sin\theta_{cs} + g\sin I\csc^2\theta_{cs}\cos\phi_{cs}\right)\left(-g\sin I\cos\phi_{cs}\right). \qquad (16)$$

When t_s is large, we can simplify Eq. (15) to

$$\lambda \approx -\frac{\cos\theta_{cs}}{t_s} \pm \sqrt{\lambda_0^2}. \qquad (17)$$

The stability depends only on the real part of λ in Eq. (17). λ_0^2 is a generalization of Eq. (A4) in, Su & Lai (2020) and generally has the same behavior: it is negative for CSs 1–3 and positive for CS4, as shown in Fig. 4. Thus, CS4 is always unstable, as there will always be at least one positive solution for λ, and the stability of CSs 1–3 are solely determined by the sign of $\cos\theta_{cs}$. Evaluating at each of the CSs (see Fig. 1), we conclude that CS1 and CS2 are stable and attracting while CS3, stable in the absence of the torque, becomes unstable. These calculations justify results long used in CS literature (e.g. Ward 1975; Fabrycky et al. 2007).

Figure 5. Plot illustrating the asymptotic behavior of initial conditions for $\eta = 0.2$ and $I = 20°$. Each dot represents an initial spin orientation, and the coloring of the dot indicates which Cassini State (legend) the system asymptotes towards.

perturbation causes systems to transition among unchanging phase space zones.

3.2.1 Analytical Calculation of Resonance Capture Probability

The specific probabilities of the two outcomes upon separatrix encounter, a zone III-II or a zone III-I transition, can be calculated analytically. Figure 6 shows how the perturbative alignment torque generates probabilistic outcomes upon separatrix encounter. We present the interpretation of Figure 6 and the calculation of the resonance capture probability by first giving a qualitative description of the intuition behind the method, then presenting a calculation in good agreement with numerical results.

We first describe the origin of the boundaries between regions of phase space that shown in Fig. 6. They are calculated numerically by integrating a point infinitesimally close to CS4 forward and backward in time. In the absence of the alignment torque, these trajectories would evolve along the separatrix, but in the presence of the alignment torque they are perturbed slightly and cease to overlap. It can be seen in Fig. 6 that this splitting opens a path from zone III into both zones I and II.

To understand this process quantitatively, as well as associate probabilities to the two possible outcomes, it is important to be more quantitative. The correct approach is to consider the evolution of the value of the *unperturbed* Hamiltonian (Eq. 8) as the spin evolves with the alignment torque. A point in zone III evolves such that H is increasing until $H \approx H_{\text{sep}}$ where H_{sep} is the value of H along the separatrix, given by

$$H_{\text{sep}} \equiv H\left(\cos\theta_4, \phi_4\right),$$

$$\approx g\sin I + \frac{g^2}{2\alpha}\cos^2 I + O\left(\eta^2\right), \tag{18}$$

where θ_4 and ϕ_4 are the coordinates of CS4. As the system evolves closer to the separatrix, the change in H over each circulation cycle can be approximated by ΔH_-, the change in H along C_- (see Fig. 2). In general, we can compute $\Delta H_\pm$ the change over both legs of the

separatrix with

$$\Delta H_\pm \equiv \oint_{C_\pm} \frac{\mathrm{d}H}{\mathrm{d}t}\,\mathrm{d}t. \tag{19}$$

This can be simplified by using:

$$\frac{\mathrm{d}H}{\mathrm{d}t} = \frac{\partial H}{\partial(\cos\theta)}\frac{\mathrm{d}(\cos\theta)}{\mathrm{d}t} + \frac{\partial H}{\partial\phi}\frac{\mathrm{d}\phi}{\mathrm{d}t},$$

$$= \left(\frac{\mathrm{d}(\cos\theta)}{\mathrm{d}t}\right)_{\text{tide}}\frac{\mathrm{d}\phi}{\mathrm{d}t}, \tag{20}$$

$$\Delta H_\pm = \mp\frac{1}{t_{\text{s}}}\int_0^{2\pi}\sin^2\theta\,\mathrm{d}\phi. \tag{21}$$

Thus, if we evaluate H every time that a trajectory crosses $\phi = 0$, we see that it will initially be negative and increase for each circulation cycle until the system encounters the separatrix. At the beginning of the separatrix-crossing orbit, the initial value of H, denoted H_{i}, satisfies $H_{\text{sep}} - \Delta H_- \leq H_{\text{i}} \leq H_{\text{sep}}$: if it is less than the lower bound, it will not cross the separatrix on this orbit, and if it is greater than the upper bound then it is already inside the separatrix. The two endpoints of this range are denoted in Fig. 8 by the black dot and cross at the left and right edges of the plot.

During the separatrix-crossing orbit, the trajectory first evolves approximately along C_- then along C_+, after which two possible outcomes can occur:

- If the final value of H at the end of this separatrix traversal, denoted H_{f}, satisfies $H_{\text{f}} > H_{\text{sep}}$, then the trajectory enters the separatrix, following the red shaded region in Fig. 8, and executes a zone III $\rightarrow$ II transition.

- If $H_{\text{f}} < H_{\text{sep}}$, then the trajectory exits the separatrix above CS4, following the yellow shaded region in Fig. 8 and executes a zone III $\rightarrow$ I transition.

Since $H_{\text{f}} = H_{\text{i}} + \Delta H_+ + \Delta H_-$, we find that if H_{i} is in the interval $\left[H_{\text{sep}} - \Delta H_-, H_{\text{sep}} - \Delta H_- - \Delta H_+\right]$, then the system executes a III $\rightarrow$ I transition, and if it is in the interval $\left[H_{\text{sep}} - \Delta H_- - \Delta H_+, H_{\text{sep}}\right]$, then the system executes a III $\rightarrow$ II transition. The values of $\cos\theta$ for which H is equal to $H_{\text{sep}} - \Delta H_-, H_{\text{sep}} - \Delta H_- - \Delta H_+$, and H_{sep} (CS4) for $\phi = 0$ are shown in Fig. 8 as the black cross, star, and dot at $\phi = 0$ respectively. Finally, if the alignment torque is weak, then $\Delta H_- \sim O\left(t_{\text{s}}^{-1}\right)$ is small compared to the characteristic values of H, and H_{i} can be effectively considered as uniformly distributed over $\left[H_{\text{sep}} - \Delta H_-, H_{\text{sep}}\right]$. As such, we obtain that

$$P_{\text{III}\rightarrow\text{II}} = \frac{\Delta H_- + \Delta H_+}{\Delta H_-}. \tag{22}$$

To actually evaluate Eq. (22), we use the parameterization for the separatrix (Su & Lai 2020) for $\eta \ll 1$:

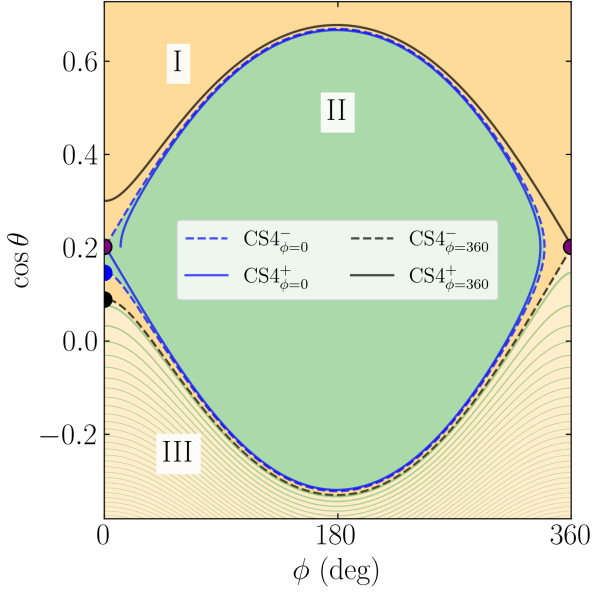$$(\cos\theta)_{C_\pm} \approx \eta\cos I \pm \sqrt{2\eta\sin I\left(1 - \cos\phi\right)}. \tag{23}$$

It can then be shown that

$$\Delta H_- \approx \frac{2\pi}{t_{\text{s}}}\left(1 - 2\eta\sin I\right) + O(\eta^{3/2}), \tag{24}$$

$$\Delta H_+ + \Delta H_- \approx \frac{32\eta^{3/2}\cos I\sqrt{\sin I}}{t_{\text{s}}} + O\left(\eta^{5/2}\right), \tag{25}$$

$$P_{\text{III}\rightarrow\text{II}} \approx \frac{16\eta^{3/2}\cos I\sqrt{\sin I}}{\pi\left(1 - 2\eta\sin I\right)}. \tag{26}$$

To directly compare Eq. (26) with numerical simulation, we perform integrations of Eqs. (10–11) while restricting our attention to

Figure 6. Plot illustrating the probabilistic origin of separatrix capture for $\eta = 0.2$, $I = 20°$, and $|gt_s| = 10^{-3}$. Orange regions converge to CS1, and green to CS2, while CS4 is labeled with the purple dots. The boundaries separating the CS1 and CS2-approaching regions consist of the critical trajectories (labeled in the legend) that, when evolved either forwards or backwards in time (superscripts in the legend labels), asymptotically approach CS4 where either $\phi = 0°$ or $\phi = 360°$ (subscripts in the legend labels). Within zone III, the regions of phase space reaching CS1 and CS2 both become very thin (shown qualitatively as the light green lines of decreasing width), reflecting the fact that the outcome for a particular initial condition can be approximated as probabilistic sufficiently far from the separatrix. Labeled in the blue and black dots at the left edge of the plot are the two backwards-in-time critical trajectories intersect $\phi = 0$, and are where H is equal to $H_{sep} - \Delta H_- - \Delta H_+$ and $H_{sep} - \Delta H_-$ respectively (Eqs. 18 and 19).

only outcomes of initial conditions in zone III. In Fig. 7, we display Eq. (26) alongside the computed $P_{III \to II}$ using 1000 initial conditions in zone III for each of 60 values of η. Excellent agreement is observed.

Finally, we remark that the calculation above is just a descriptive application of *Melnikov's Method* (Guckenheimer & Holmes 1983). Melnikov's Method is a general calculation that gives the degree of splitting of a "homoclinic orbit" (here, the separatrix) induced by a small, possibly time-dependent, perturbation. The explicit connection between the evolution of the unperturbed Hamiltonian and distances between curves in phase space (as seen in Fig. 8) is provided by Melnikov's Method.

4 SPIN EVOLUTION WITH WEAK TIDAL FRICTION

4.1 Tidal Model: Equilibrium Tides

To model the dissipative effect of times, we use the weak friction theory of equilibrium tides (Lai 2012). In this model, tides cause
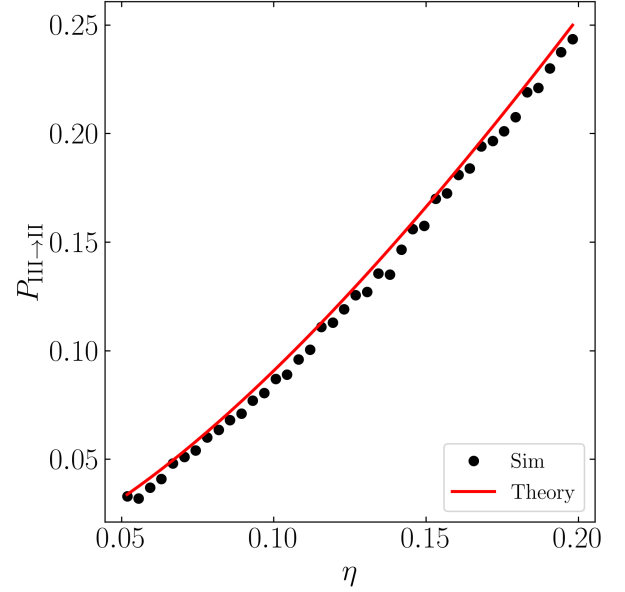
Figure 7. Plot of $P_{III \to II}$ as a function of η for the constant alignment torque model considered in Section 3. For each η, 1000 initial θ_0 in zone III are evolved until just after separatrix encounter, where the outcome of the encounter is recorded. Shown in red is Eq. (26).

both $\hat{s}$ and Ω_s to evolve on the characteristic tidal timescale t_a:

$$\left(\frac{d\hat{s}}{dt}\right)_{tide} = \frac{1}{t_a} \left[\frac{2n}{\Omega_s} - \left(\hat{s} \cdot \hat{l}\right)\right] \hat{s} \times \left(\hat{l} \times \hat{s}\right), \tag{27}$$

$$\frac{1}{\Omega_s}\left(\frac{d\Omega_s}{dt}\right)_{tide} = \frac{1}{t_a}\left[\frac{2n}{\Omega_s}\left(\hat{s} \cdot \hat{l}\right) - 1 - \left(\hat{s} \cdot \hat{l}\right)^2\right], \tag{28}$$

where t_a is given by

$$\frac{1}{t_a} \equiv \frac{L}{2S}\frac{\Omega_s}{2n}\frac{3k_2}{Q}\left(\frac{M_\star}{m}\right)\left(\frac{R}{a}\right)^5 n. \tag{29}$$

Here, $L = ma^2 n$ and $S = kmR^2\Omega_s$ are the orbital and spin angular momenta of the inner planet, respectively. We neglect orbital evolution in this section since the time scale is longer than t_a by a factor of $\sim L/S \gg 1$, and so t_a is a constant. We will continue mostly consider the case where $|gt_a| \gg 1$. The full equations of motion including weak tidal friction are

$$\frac{d\theta}{dt} = g \sin I \sin \phi - \frac{1}{t_a}\sin\theta\left(\frac{2n}{\Omega_s} - \cos\theta\right), \tag{30}$$

$$\frac{d\phi}{dt} = -\alpha\cos\theta - g\left(\cos I + \sin I \cot\theta\cos\phi\right), \tag{31}$$

$$\frac{1}{\Omega_s}\frac{d\Omega_s}{dt} = \frac{1}{t_a}\left[\frac{2n}{\Omega_s}\cos\theta - \left(1 + \cos^2\theta\right)\right]. \tag{32}$$
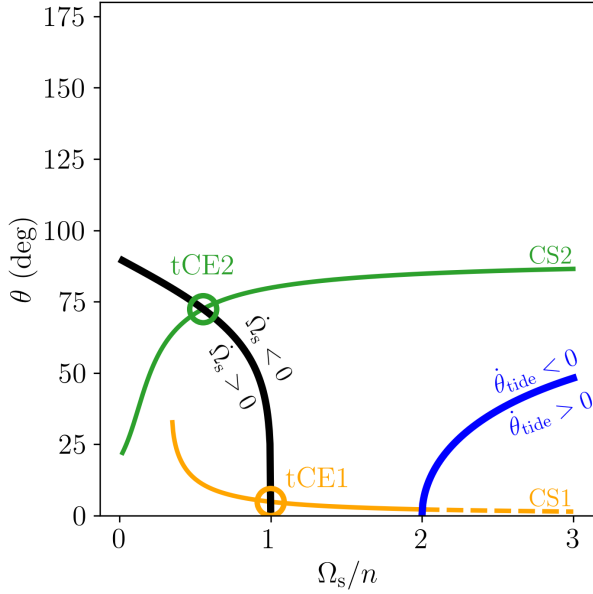
The conditions for which the two tidal terms vanish can be respectively expressed as:

$$\dot{\theta}_{tide} = 0: \quad \frac{2n}{\Omega_s} = \cos\theta, \tag{33}$$

$$\dot{\Omega}_s = 0: \quad \frac{n}{\Omega_s} = \frac{1 + \cos^2\theta}{2\cos\theta}. \tag{34}$$

To understand the long-term behaviors of the system, we first consider its behavior near a CS. Specifically, we wish to understand

Figure 8. Schematic depiction of the effect of tidal friction on the planet's spin for $I = 20°$ and $\eta_{sync} = 0.2$. The black and blue lines denote where the tidal $\dot{\Omega}_s$ and $\dot{\theta}$ change signs (Eqs. 33–34). The orange and green lines give the CS1 and CS2 obliquities respectively, which are the two CSs that are stable under the effect of tidal dissipation. Note that when $\dot{\theta}_{tide} > 0$, CS1 becomes unstable, denoted by the dashed orange line. The points that are both CSs and satisfy $\dot{\Omega}_s = 0$ are the tidal Cassini Equilibria (tCE), which are circled and labeled.

whether initial conditions near a CS stay near the CS as the evolution of Ω_s causes the CSs to evolve. We first note that the evolution of Ω_s does not drive spins towards or away from CSs: as long as it evolves sufficiently slowly (adiabatically, Su & Lai 2020), conservation of phase space area ensures that trajectories will remain at a roughly fixed distance to stable equilibria of the system. Thus, Eq. (27) alone determines whether a point evolves towards or away from a nearby CS as Ω_s evolves. Then, evaluating Eq. (17) with $t_s = t_a/(2n/\Omega_s - \cos\theta)$ (compare Eqs. 9 and Eq. 27), we see that CS2 is still always stable, while CS1 is becomes unstable for $\Omega_s > 2n$.

Using this result, we can then identify the long-term equilibria of the system (i.e. when including the evolution of Ω_s), as the long-term equilibria of the system must both satisfy $\dot{\Omega}_s = 0$ and be a stable CS. Figure 8 describes Eqs. (27–28) qualitatively in the coordinates (Ω_s, θ), along with the locations of CS1 and CS2. The two circled points in Fig. 8 satisfy the criteria to be long-term equilibria, and we call them *tidal Cassini Equilibria* (tCE). We number tCE1 and tCE2 the tCE that are in CSs 1 and 2 respectively. The obliquities of the tCE depend on the system architecture, which can be quantified using the parameter

$$\eta_{sync} \equiv (\eta)_{\Omega_s=n}, \tag{35}$$

The tCE obliquity as a function of η_{sync} are shown for $I = 20°$ in the top panel of Fig. 14 and for $I = 5°$ in the top panel of Fig. 15.

There are two important conditions that change the existence and stability of the tCE. First, if $\eta_{sync} > \eta_c$, then tCE1 will not exist[1].

---

[1] Strictly speaking, η_{sync} can be slightly smaller than η_c, as the planet's spin is slightly subsynchronous at tCE1 when $\eta \approx \eta_c$, see Fig. 8.

Secondly, tCE2 may not be stable if the tidal phase shift is too large. Applying the results of Section 3.1, we find that tCE2 is stable as long as $t_a \geq t_{a,c}$ where

$$t_{a,c} \equiv \frac{\sin\theta_{tCE2}}{|g|\sin I}. \tag{36}$$

The tCE2 subscripts denote evaluation at tCE2. This can be further simplified using that Eq. (34) and $\cos\theta \approx \eta\cos I$ are satisfied at tCE2, giving:

$$t_{a,c} \approx \frac{1}{|g|\sin I}\sqrt{\frac{2}{\eta_{sync}\cos I}}. \tag{37}$$

4.2 Spin Obliquity Evolution as a Function of Initial Spin Orientation

With this result, we can now consider the final fate of the inner planet's spin. We assume that the planet is initially rotating supersynchronously and adopt the fiducial initial spin frequency $\Omega_{s,i} = 10n$. The final results are not sensitive on the specific initial spin as long as $\Omega_{s,i} \gg n$. Then, for a given initial θ_0 and ϕ_0, the final outcome (either tCE1 and tCE2) of the system can be calculated by direct integration of Eqs. (5, 27–28). In Fig. 9, we show the final outcome for many randomly chosen θ_0 and ϕ_0 for $\eta_{sync} = 0.06$ and $I = 20°$. We see that tCE1 is generally reached for spins initially in zone I, tCE2 is generally reached for spins initially in zone II, and a probabilistic outcome is observed for spins initially in zone III, very similar to the results found for the alignment torque in Section 3. Figures 10 and 11 show the same results but for $\eta_{sync} = 0.2$ and $\eta_{sync} = 0.5$. As η_{sync} is increased, more initial conditions reach tCE2. This is both because there are more systems initially in zone II and because more systems initially in zone III execute a III → II transition upon separatrix encounter. Note also that in Fig. 11, even initial conditions in zone I are able to reach tCE2; we comment on the origin of this behavior in the next section.

4.2.1 Analytical Calculation of Resonance Capture Probability

Even when including the evolution of Ω_s, and therefore the spin-orbit precession frequency α, the probabilities of the III → I and III → II transitions upon separatrix encounter can be computed. The calculation is more involved than that presented in Section 3.2, and also incorporates the seminal resonance capture theory of Henrard (1982). In this section, we give an overview of the approach.

In Section 3.2, we found that keeping track of the value of H, the value of the unperturbed Hamiltonian, allowed us to calculate the probabilities of the various outcomes of separatrix encounter. Specifically, the outcome upon separatrix encounter is determined by the value of H at the start of the separatrix-crossing orbit relative to H_{sep}, the value of H along the separatrix. When the spin is also evolving, H_{sep} is also changing during the separatrix-crossing orbit, and the discussion in Section 3.2 must be generalized to account for this. Instead of focusing on the evolution of H along a trajectory, we instead follow the evolution of

$$K \equiv H - H_{sep}. \tag{38}$$

Note that $K > 0$ inside the separatrix, and $K < 0$ outside. Then, the outcome of the separatrix-crossing orbit is largely the same as discussed in Section 3.2. First, we must compute the change in K along the legs of the separatrix. We define $\Delta K_{\pm}$ by generalizing
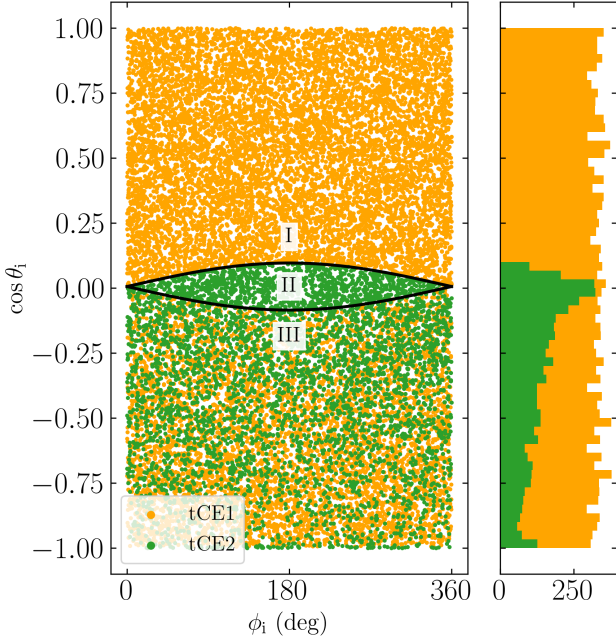
Figure 9. *Left:* Each dot indicates which tCE a given initial condition (θ_i, ϕ_i) evolve towards (labeled in legend), for $\eta_{\rm sync} = 0.06$ and $I = 20°$. The separatrix is shown as the black line. Note that points above the separatrix evolve towards tCE1, points inside the separatrix evolve towards tCE2, and points below the separatrix have a probabilistic outcome. *Right:* Histogram of which tCE a given initial obliquity θ_i evolves towards.
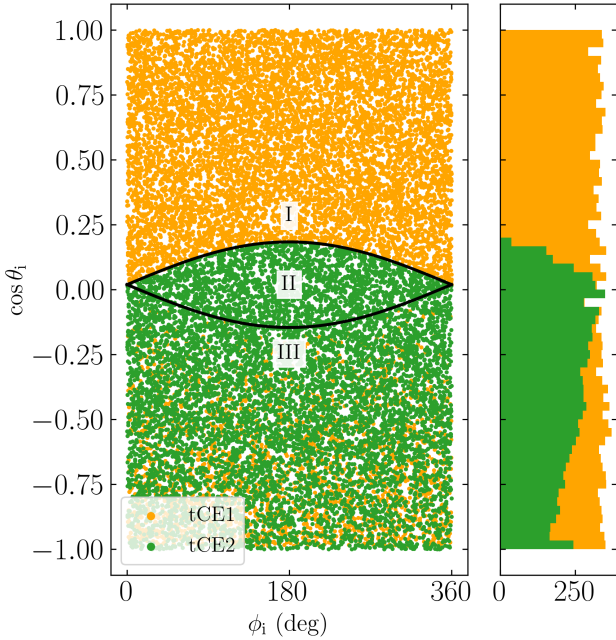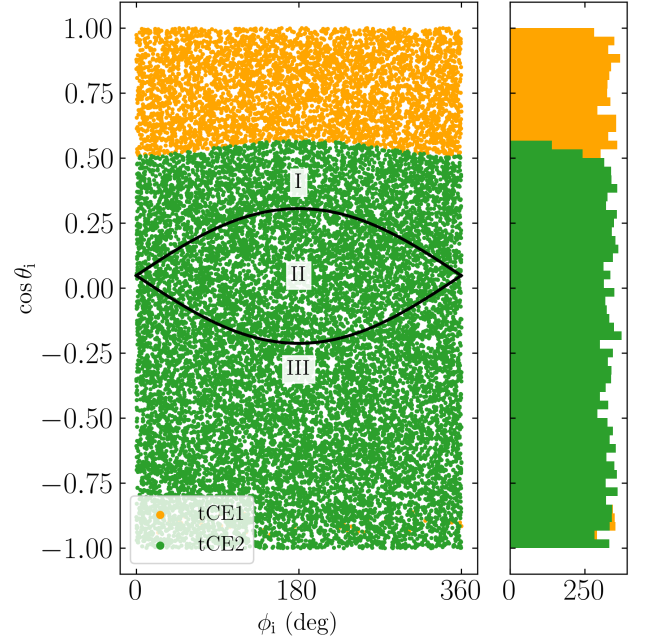
Figure 11. Same as Fig. 9 but for $\eta_{\rm sync} = 0.7$. Note that even points above the separatrix can evolve towards tCE2 here.

Eq. (19) very naturally:

$$\Delta K_{\pm} = \oint_{C_{\pm}} \frac{\mathrm{d}H}{\mathrm{d}t} - \frac{\mathrm{d}H_{\rm sep}}{\mathrm{d}t} \, \mathrm{d}t. \tag{39}$$

Here, however, note that $C_{\pm}$ depends on the value of $\Omega_{\rm s}$ upon separatrix encounter. Since there is no closed form solution for $\Omega_{\rm s}(t)$, the probabilities of the various outcomes can only be determined as a function of the system properties at separatrix encounter, and not as a simple function of the initial conditions.

Then, if we call K_i the value of K at the start ($\phi = 0$) of the separatrix-crossing orbit, $K_i > -\Delta K_+ - \Delta K_-$ gives a III → II transition and eventual evolution towards tCE2 while $-\Delta K_- < K_i < -\Delta K_- - \Delta K_+$ gives a III → I transition and ultimate evolution towards tCE1. Thus, we find that the probability of a III → II transition is given by

$$P_{\rm III \to II} = \frac{\Delta K_+ + \Delta K_-}{\Delta K_-}. \tag{40}$$

Since $\Delta K_{\pm}$ are evaluated at resonance encounter, and $\Omega_{\rm s}$ is evolving, there is no way to express $\Delta K_{\pm}$ as a closed form of initial conditions. In fact, since many resonance encounters occur when η is substantial, even an approximate calculation using Eq. (23) is inaccurate, and we instead calculate $\Delta K_{\pm}$ along the two legs of the separatrix obtained numerically via a root finding algorithm. Note that Eqs. (39, 40) are equivalent to the separatrix capture result of Henrard (1982) when $\cos \theta$ is not evolving (Henrard & Murigande 1987). Here, we have argued that this classic calculation can be unified with the calculation given in Section 3.2 to give an accurate prediction of separatrix encounter outcome probabilities in the presence of both a dissipative perturbation and a parametric variation of the Hamiltonian.

To validate the accuracy of Eq. (40), we can compare with the numerical integration of Eqs. (5, 27–28) for many initial conditions in zone III while evaluating $P_{\rm III \to II}$ (and thus also obtaining $P_{\rm III \to I} = 1 - P_{\rm III \to II}$) for each simulation at the moment it encounters the separatrix. If the theory is correct, the total numbers of systems

**Figure 10.** Same as Fig. 9 but for $\eta_{\rm sync} = 0.2$.
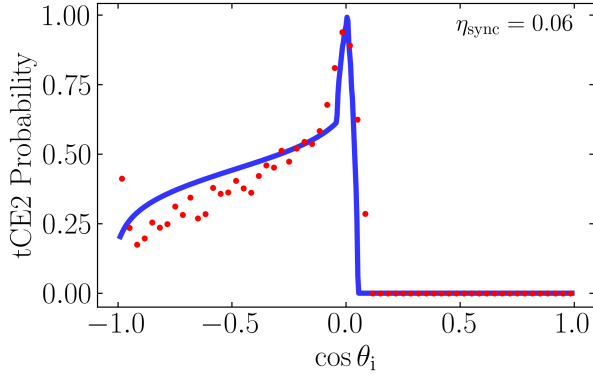
Figure 12. Comparison of the fraction of systems converging to tCE2 obtained via numerical simulation (red dots) and obtained via a semi-analytic calculation (blue line) for $\eta_{\text{sync}} = 0.06$ and $I = 20°$ (see right panel of Fig. 9). The semi-analytic calculation is performed by numerically integrating Eqs. (5, 27–28) on a grid of initial conditions uniform in $\cos \theta_i$ and ϕ_i until the system reaches the separatrix, then calculating the probability of reaching tCE2 for each integration using Eq. (40).
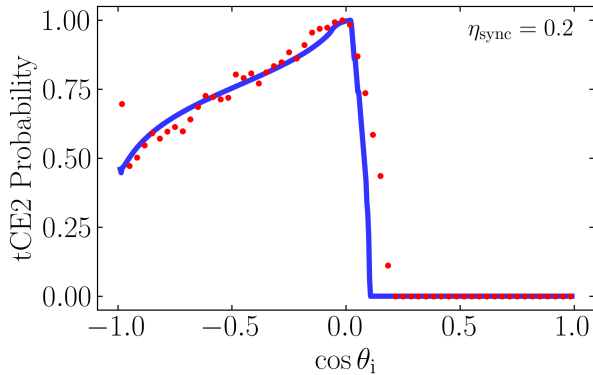
Figure 13. Same as Fig. 12 but for $\eta_{\text{sync}} = 0.2$, corresponding to the right panel of Fig. 10.

converging to each of tCE1 and tCE2 should be equal to those predicted by the sums of the calculated probabilities. In Fig. 12, we show the agreement of this semi-analytic procedure with the numerical results displayed earlier in the right panel of Fig. 9. Good agreement is observed. Figs. 13 shows the same for Figs. 10. Mostly satisfactory agreement is observed. Thus, we conclude that the outcomes of separatrix encounter are accurately predicted by Eq. (40).

With the above calculation, we can understand why even initial conditions in zone I can converge to tCE2. As long as the inital spin is sufficiently large ($\geq 2n$), Eq. (27) shows that sufficiently large initial obliquities are *increased* by weak tidal friction (see the bottom right region of Fig. 8). This increase means that even initial conditions in zone I can sometimes be driven by weak tidal friction to experience separatrix encounter. When this is the case, it can be shown that both $\Delta K_+ > 0$ and $\Delta K_- > 0$. This implies that both III → II and I → II outcomes are guaranteed, and thus initial conditions in all three zones can evolve into tCE2.
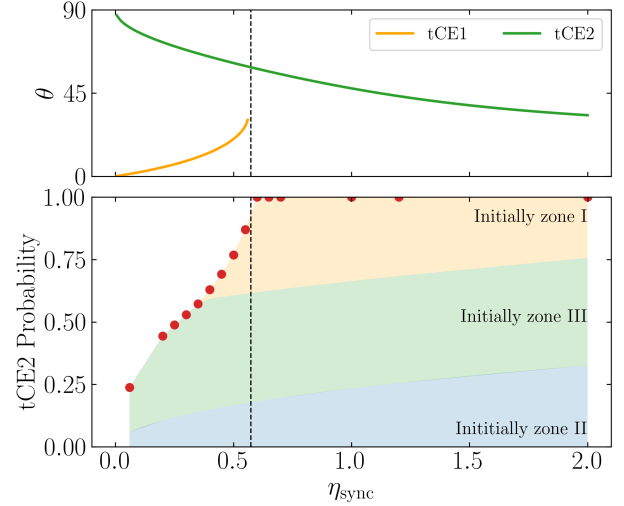
Figure 14. *Top:* Obliquities of the two tCE where $I = 20°$ for a range of η_{sync} (Eq. 35), averaged over an isotropic initial spin orientation. *Bottom:* Total probability of ending up in tCE2 (red dots). The red shaded region denotes the contribution of initial conditions in zone II that converge to tCE2 directly, and the yellow shaded region denotes the contribution of initial conditions in zone III that converge to tCE2 after a separatrix encounter. The vertical dashed line denotes η_c (Eq. 7).

4.3 Spin Obliquity Evolution as a Function of Precession Strength

In the previous section, we considered the outcome as a function of the initial spin orientation, specified by θ_0 and ϕ_0. In this section, we consider the distribution of outcomes when averaging over a distribution of initial spin orientations. For simplicity, we just consider $\hat{s}$ being isotropically distributed. Figure 14 shows this for $I = 20°$ as a function of η_{sync}. It can be seen that tCE2 is reached with substantial probability ($\sim 50°$) while it is also at a substantial obliquity ($\sim 60°$) for $\eta_{\text{sync}} \approx 0.4$. Furthermore, the bottom panel illustrates that initial conditions other than those beginning in zone II generate a significant fraction of systems that converge to tCE2.
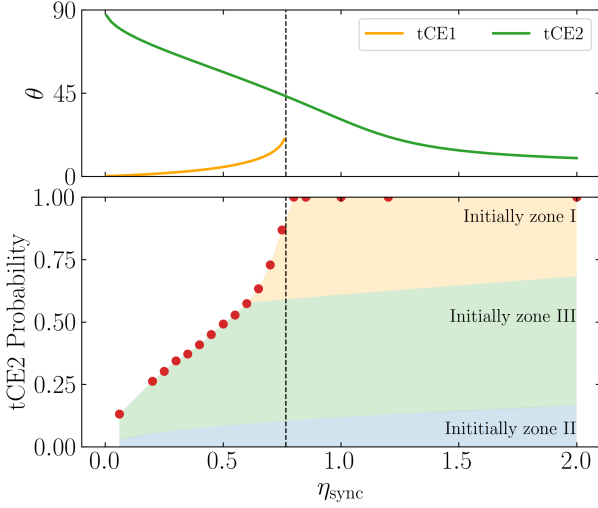
5 APPLICATIONS

5.1 Application to Warm + Cold Jupiter Systems

Consider a system consisting of an inner Super-Earth (SE) and an exterior cold Jupiter (CJ); such systems are expected to be abundant (Zhu & Wu 2018). For this system, the relative tidal dissipation rate $|gt_a|^{-1}$ can be computed

$$\frac{1}{|gt_a|} \approx 0.003 \frac{1}{\cos I} \left(\frac{2k_2/Q}{10^{-3}} \right) \left(\frac{m_p}{M_J} \right)^{-1} \left(\frac{a_p}{5 \text{ AU}} \right)^3$$
$$\times \left(\frac{a}{0.4 \text{ AU}} \right)^{-6} \left(\frac{\rho}{3 \text{ g/cm}^3} \right)^{-1} \left(\frac{M_\star}{M_\odot} \right)^2. \quad (41)$$

In physical units, $t_a \sim 2 \times 10^8$ yr for the parameters adopted above, and $\dot{a}/a \sim 10^{14}$ yr, so the spin evolution of the inner planet occurs within the characteristic age of most planetary systems, while the orbital evolution of the inner planet can indeed by safely neglected. Thus, the approximations of slow tidal dissipation and constant a

Figure 15. Same as Fig. 14 but for $I = 5°$.

Figure 16. Plot showing allowable parameter space for USP formation for the fiducial parameters: $P_{j+1}/P_j = 1.3$ and $M_\star = M_\odot$, mirroring Figure 5 of Millholland & Spalding (2020). Shaded in blue is their region of allowable parameter space for USP formation ($\eta_{\rm sync} \geq 1$ and $\dot{a}/a <$ Gyr), while shaded in green is the region where $\eta_{\rm sync} \geq 1/3$, for which the tCE2 probability is > 50% for $I = 20°$ (see Fig. 14). I added a few fudge factors temporarily to be a little bit to be closer to the Millholland plot; I will double check their validity and update this plot to better reflect our actual numbers / parameters.

used throughout Section 4 is valid. For the same fiducial parameters, Eq. (35) can be evaluated

$$\eta_{\rm sync} = 0.33 \left(\frac{k}{k_{\rm q}}\right)\left(\frac{m_{\rm p}}{M_{\rm J}}\right)\left(\frac{a_{\rm p}}{5~{\rm AU}}\right)^{-3}$$
$$\times \left(\frac{a}{0.4~{\rm AU}}\right)^6 \left(\frac{\rho}{3~{\rm g/cm^3}}\right)\left(\frac{M_\star}{M_\odot}\right)^{-2}. \quad (42)$$

Here, $\rho = m/\left(4\pi R^3/3\right)$ is the average density of the inner planet, and $M_{\rm J}$ is the mass of Jupiter. From Figs. 14 and 15, we see that this value of $\eta_{\rm sync}$ gives a high-obliquity tCE2 with significant probability. Thus, we predict that a sizable fraction of SEs with exterior CJ companions can have significant obliquities ($\sim\gtrsim 30°$).
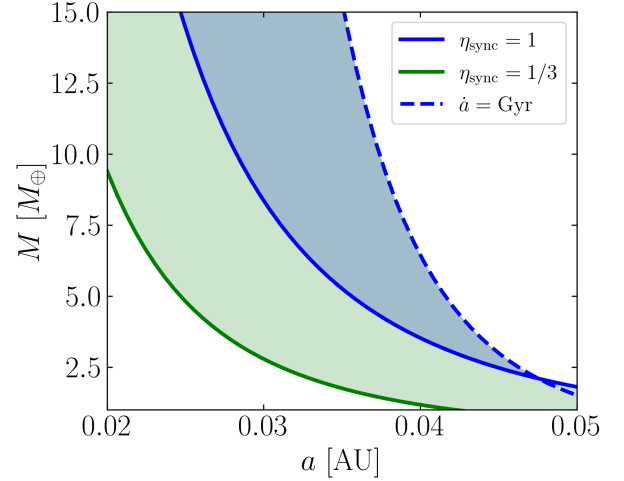
5.2 Application to Ultra-short-period Planet Formation

In Millholland & Spalding (2020), the authors consider capture into the CS2 resonance as part of a mechanism to induce ultra-short period planet (USP) formation. They envision a process consisting of three stages: (i) capture into CS2, (ii) simultaneous inward tidal migration and increase of the obliquity of CS2, and (iii) destruction of CS2 due to strong tidal dissipation and stalling of inward migration. Below, we revisit this process and show that the parameter space for this obliquity-driven tidal runaway formation channel of USPs is larger than is given in their work.

First, we verify agreement of our criterion for breaking of CS2 with theirs. Evaluating Eq. (13) for the weak tidal friction torque given by Eq. (12), we find that tCE2 breaks when the semi-major axis is smaller than $a_{\rm break}$ where I haven't double checked this calculation. . .

$$a_{\rm break} \approx 0.01~{\rm AU} \left(\frac{k}{k_q}\right)^{-1/18} \left(\frac{2k_2/Q}{10^{-3}}\right)^{1/9} \left(\frac{m_{\rm p}}{M_\oplus}\right)^{-1/6}$$
$$\times \left(\frac{a_{\rm p}}{0.05~{\rm AU}}\right)^{1/2} \left(\frac{\rho}{6~{\rm g/cm^3}}\right)^{-1/6} \left(\frac{M_\star}{M_\odot}\right)^{1/3}. \quad (43)$$

We have calculated this for a mutual inclination of $I = 5°$. This corresponds to an orbital period of about half a day, qualifying as a USP.

Second, we note that Millholland & Spalding (2020) focus on system architectures for which $\eta_{\rm sync} \gtrsim \eta_{\rm c}$ (where CS1 does not exist at spin-orbit synchronization; see Eqs. 7 and 35), finding that architectures for which $\eta_{\rm sync} \lesssim \eta_{\rm c}$ always generate evolution towards CS1. However, they assumed an initial obliquity $\theta_0 = 0°$, while broader distributions of initial planet obliquities will give some probability of evolution towards CS2 and tCE2 (see Figs. 9–11). Thus, it is not necessary to restrict formation of USPs via tidal runaway to system architectures for which $\eta_{\rm sync} \gtrsim \eta_{\rm c}$. In fig

In particular, architectures with larger period ratios P_{j+1}/P_j (and thus, semi-major axis ratios; see Eq. 35) are still able to undergo tidal runaway. Such architectures can be advantageous for USP formation as more of their total angular momentum budget is in the outer planet's orbit, allowing for additional migration (Fabrycky et al. 2007; Millholland & Spalding 2020).

5.3 Application to WASP-12b

Thoughts:

• Significantly limited by conservation of angular momentum (spin of the star is a reservoir?).

• Initial conditions are solidly in the $\eta_{\rm sync} \gg 1$ regime (CS2 obliquity goes to near zero when a is increased by $\sim 30\%$), probably not a very useful application of our theory. For systems where the perturber is *strong*, our theory produces extra tCE2 systems compared to neglecting the effect of resonance capture, but where the perturber is weak, everybody knows that CS2 is guaranteed.

6 SUMMARY AND DISCUSSION

7 ACKNOWLEDGEMENTS

REFERENCES

Anderson, K. R., & Lai, D. 2018, Monthly Notices of the Royal Astronomical Society, 480, 1402

Colombo, G. 1966, SAO Special Report, 203

Fabrycky, D. C., Johnson, E. T., & Goodman, J. 2007, The Astrophysical Journal, 665, 754

Guckenheimer, J., & Holmes, P. J. 1983, Nonlinear oscillations, dynamical systems, and bifurcations of vector fields (New York: Springer-Verlag)

Henrard, J. 1982, Celestial Mechanics and Dynamical Astronomy, 27, 3

Henrard, J., & Murigande, C. 1987, Celestial Mechanics, 40, 345

Lai, D. 2012, Monthly Notices of the Royal Astronomical Society, 423, 486

Lainey, V. 2016, Celestial Mechanics and Dynamical Astronomy, 126, 145

Millholland, S., & Batygin, K. 2019, The Astrophysical Journal, 876, 119

Millholland, S. C., & Spalding, C. 2020, The Astrophysical Journal, 905, 71

Peale, S. J. 1969, The Astronomical Journal, 74, 483

Su, Y., & Lai, D. 2020, arXiv preprint arXiv:2004.14380

Ward, W. R. 1975, The Astronomical Journal, 80, 64

Zhu, W., & Wu, Y. 2018, The Astronomical Journal, 156, 92

APPENDIX A: CONVERGENCE OF INITIAL CONDITIONS INSIDE THE SEPARATRIX TO CS2

In Section 3.1, we studied the stability of the CSs under of tidal alignment torque given by Eq. (9), finding that CS2 is locally stable. Later, in Section 3.2, we found that all initial conditions within the separatrix converge to CS2, which is not guaranteed by local stability of CS2. In this section, we give an analytic demonstration that all points inside the separatrix indeed converge to CS2, focusing on the case where $\eta \ll 1$.

Similarly to the analytic calculation in Section 3.2, we seek to compute the change in the unperturbed Hamiltonian over a single libration cycle. To calculate the evolution of H, we first parameterize the unperturbed trajectory (similarly to Eq. 23). For initial conditions inside the separatrix, the value of H can be written $H = H_{\mathrm{sep}} + \Delta H$ where $\Delta H > 0$, and the two legs of the libration trajectory can be written:

$$\cos \theta_\pm \approx \eta \cos I \pm \sqrt{2\eta \left[\sin I \left(1 - \cos \phi\right) - \Delta H\right]}. \tag{A1}$$

We have taken $\sin \theta \approx 1$, a good approximation in zone II when $\eta \ll 1$. Note that there are some values of ϕ for which no solutions of θ exist, reflecting the fact that the libration cycle does not extend over the full interval $\phi \in [0, 2\pi]$. During a libration cycle, θ_- $[\theta_+]$ is traversed while $\phi' > 0$ $[\phi' < 0]$, i.e. the trajectory librates counterclockwise in $(\cos \theta, \phi)$ phase space (see Fig. 2).

The leading order change to H over a single libration cycle can then computed by integrating $\mathrm{d}H/\mathrm{d}t$ along this trajectory, yielding:

$$
\begin{aligned}
\oint \frac{\mathrm{d}H}{\mathrm{d}t}\, \mathrm{d}t &= \oint \left(\frac{\mathrm{d}(\cos \theta)}{\mathrm{d}t}\right)_{\mathrm{tide}} \mathrm{d}\phi, \\
&= \int_{\phi_{\min}}^{\phi_{\max}} \frac{1}{t_{\mathrm{s}}} \left(\sin^2 \theta_- - \sin^2 \theta_+\right)\, \mathrm{d}\phi \\
&= \frac{1}{t_{\mathrm{s}}} \int_{\phi_{\min}}^{\phi_{\max}} 4\eta \cos I \sqrt{2\eta \left[\sin I \left(1 - \cos \phi\right) - \Delta H\right]}\, \mathrm{d}\phi > 0.
\end{aligned}
\tag{A2}
$$

Here, $\phi_{\min} > 0$ and $\phi_{\max} < 2\pi$ are defined such that the trajectory librates over $\phi \in [\phi_{\min}, \phi_{\max}]$. Thus, H is strictly increasing for all initial conditions inside the separatrix, and they all converge to CS2.